Influence of Interlayer Stacking on Optical Behavior in WSe_2/MoS_2 van der Waals Heterostructures

Widad Louafi,[1] Karim Rezouali,[1,2,3] Daniele Varsano,[4,5] Maurizia Palummo,[6,5] Maurits W. Haverkort,[7] and Samir Lounis[8,3]

[1] *Laboratoire de Physique Théorique, Faculté des Sciences Exactes, Université de Bejaia, 06000 Bejaia, Algérie*
[2] *Faculty of Physics and CENIDE, University of Duisburg-Essen, D-47053 Duisburg, Germany*
[3] *Peter Grünberg Institut, Forschungszentrum Jülich and JARA, D-52425 Jülich, Germany*
[4] *Centro S3, Istituto Nanoscienze—Consiglio Nazionale delle Ricerche (CNR-NANO), via Campi 213/A, 41125 Modena, Italy*
[5] *European Theoretical Spectroscopy Facility (ETSF)*
[6] *Dipartimento di Fisica, Università di Roma 'Tor Vergata', Via della Ricerca Scientifica 1, I-00133 Roma, Italy*
[7] *Institute for Theoretical Physics, Heidelberg University, Heidelberg, Germany*
[8] *Institute of Physics, Martin-Luther-University Halle-Wittenberg, 06099 Halle (Saale), Germany*

We investigate the impact of crystal alignment on excitonic behavior in WSe_2/MoS_2 van der Waals heterostructures by comparing eclipsed (AA) and staggered (AB) stacking configurations. Our first-principles and symmetry-based analysis reveal that interlayer stacking symmetry plays a central role in determining the nature of electron-hole pairs. We uncover a rich variety of excitonic states, including spatially confined two-dimensional (2D) excitons, delocalized three-dimensional (3D) excitons, and charge-transfer (CT) excitons with interlayer character. The dimensionality and optical activity of these excitons are governed by the interplay among orbital character, interlayer hybridization, and symmetry-imposed selection rules. Our findings establish general principles for engineering excitonic properties in van der Waals heterostructures through controlled layer orientation and stacking order.

I. INTRODUCTION

Two-dimensional (2D) semiconducting materials made of transition metal dichalcogenides (TMDs) have recently gained popularity due to their intriguing physical and chemical properties, which hold promise for the next generation of optoelectronic, photonic, and energy conversion devices.[1–6]

Among others, monolayers WSe_2 and MoS_2 are two important members of these materials, composed of a hexagonal sheet of transition metal atoms (Mo, W) sandwiched between two sheets of chalcogen atoms (S, Se), which are held together by covalent bonds. The category of these two 2D materials fabricated by means of mechanical exfoliation, are finite band gap materials exhibiting direct fundamental gaps spanning the visible to near-infrared (NIR) spectrum. This characteristics enables efficient light-matter interaction[7] and opens a large avenue for applications in photodetectors,[8,9] light-emitting diodes (LEDs),[10–12] and photovoltaic devices.[13,14] The strong excitonic effects observed in these materials further enhance their optical performance, making them ideal candidates for nanoscale optoelectronic devices.[15]

A critical trait of TMDs monolayers is that their electronic and optical properties are valley-dependent, a consequence of strong spin-orbit coupling and broken inversion symmetry.[16,17] The development of valleytronics, an emerging discipline that exploits the degree of freedom of valleys for information processing and storage,[18–20] is made possible by the presence of distinct valleys at the K and K' points of the Brillouin zone.

The electronic properties of TMDs monolayers can be engineered by creating heterostructures through stacking different monolayers. These heterostructures are kept together by weak van der Waals (vdW) forces, allowing for precise control over layer composition, stacking orientation, and interlayer coupling.[1,21,22] A particularly intriguing configuration is the type-II band alignment, where the conduction band minimum (CB) of one material aligns with the valence band maximum (VB) of the adjacent layer. This staggered energy level arrangement enables the spatial separation of photoexcited charge carriers, making type-II heterojunctions worth using in photovoltaics, photodetectors, and photocatalysis.[23,24]

TMD heterostructures also exhibit efficient exciton dissociation and charge transfer processes, which are crucial to the performance of optoelectronic devices. These structures exploit the tunability of interlayer excitons, in which electrons and holes reside in distinct layers, resulting in prolonged excitonic radiative lifetime and consequently higher device efficiency.[25,26] For instance, WSe_2/MoS_2 and $WS_2/MoSe_2$ heterostructures have shown extraordinary performance in charge carrier separation and energy conversion applications.[14,2714,27] Due to the presence of type-II band alignment and tailored vdW interactions, these systems were able to produce photocurrent and harvest energy more effectively.[28,29]

Going beyond optoelectronic applications, TMD heterostructures are emerging as promising platforms for quantum technologies. Twisting adjacent TMD layers to form moiré superlattices enables the emergence of flat electronic bands, which host correlated phenomena such as Mott insulating states and superconductivity.[30,31] The Moiré potential landscape that results offers a highly tunable platform for the investigation of strong electronic correlations and quantum phase transitions, thereby em-

phasizing their potential to advance both fundamental quantum science and device engineering. Moreover, the integration of TMD heterostructures with other 2D materials, such as graphene and hexagonal boron nitride (hBN), broadens their portfolios for device layouts. Graphene, with its high electrical conductivity and flexibility, functions as an ideal electrode material, while hBN provides an atomically smooth insulating layer with minimal charge traps.[32] These hybrid systems enabled the building of innovative devices, such as tunneling transistors, vertical heterojunction diodes, and flexible electronics.[33]

In this work, we investigate the optoelectronic properties of WSe_2/MoS_2 bilayer van der Waals (vdW) periodic heterojunctions, focusing on the three stackings that correspond to local energy minima in R-type Moiré patterns.[22] Using a highly precise, state-of-the-art ab initio many-body approach, we analyze the spectra in detail and demonstrate that the nature and dimensionality of excitons in these heterojunctions can be systematically controlled. Our findings reveal the significant impact of stacking configurations on the optical excitations at the absorption onset. By systematically varying the arrangement of the WSe_2 and MoS_2 layers, we identify three distinct types of electron-hole pairs of two-dimensional (2D) intralayer excitons, three-dimensional (3D) interlayer excitons, and charge-transfer (CT) excitons. We further discuss their emergence based on symmetry considerations, providing a deeper understanding of the relationship between stacking order and excitonic properties in vdW heterostructures.

The paper is organized as follows: Section II describes the computational methods employed in this study. Section III presents and discusses our results, and Section IV summarizes the main conclusions.

II. METHOD

We performed density functional theory (DFT),[34,35] *GW*, and Bethe–Salpeter equation (BSE) formalism utilizing the Quantum Espresso[36] and Yambo[37,38] codes. This allows for a sufficiently accurate description of both the ground-state (DFT), one-particle excitation energies (*GW*), and two-particle excitonic excitations as observed in optical experiments (BSE).

We first calculated the ground-state properties utilizing DFT,[34,35] with norm-conserving pseudopotentials and a plane-wave basis set. The ionic potential was modeled using Optimized Norm-Conserving Vanderbilt (ONCV) pseudopotentials.[39] The exchange-correlation effects were treated within the generalized gradient approximation (GGA) using the Perdew-Burke-Ernzerhof (PBE) functional,[40] supplemented by the vdW-D3 correction[41] to account for long-range van der Waals interactions between monolayers. Spin-orbit coupling was included in all calculations, and the *sp* semicore states of the transition metal atoms were explicitly treated as valence electrons.[13,26,42] This approach is essential for accurately capturing the exchange contribution to the self-energy term in *GW* calculations.

For all systems, we adopted a plane-wave energy cutoff of 70 Rydberg (Ry) for the electronic wave function expansion and employed a 12 × 12 × 1 Monkhorst-Pack[43] k-point mesh for Brillouin zone (BZ) sampling. A vacuum layer of 27 Å was introduced along the out-of-plane direction to prevent spurious interactions between periodic images.

Structural relaxations were performed until the atomic forces were reduced below 0.01 eV/Å, and the energy convergence threshold was set to 10^{-5} eV. These criteria ensured that the residual stress remained below 0.01 kbar.

Since DFT, in its local and semi-local approximations, often underestimates band gaps due to its limited treatment of electron-electron interactions, we employed the more accurate GW approximation to obtain reliable quasiparticle energies. Specifically, the G_0W_0 approach was used to correct the Kohn-Sham eigenvalues by solving the Dyson equation,[44–47] thereby renormalizing the band gaps to values in better agreement with experimental measurements. The quasiparticle (QP) energies (single-particle excitation energies) were computed within the G_0W_0 by using the linearized quasiparticle equation:[48]

$$\varepsilon^{n\mathbf{k}}_{\mathbf{QP}} = \varepsilon_{n\mathbf{k}} + Z_{n\mathbf{k}}\langle n\mathbf{k}|\Sigma(\varepsilon_{n\mathbf{k}}) - v_{xc}|n\mathbf{k}\rangle \ , \qquad (1)$$

where $\epsilon_{n\mathbf{k}}$, $\phi^{KS}_{n\mathbf{k}}$ and V_{xc} describe the Kohn-Sham eigenvalues, orbitals, and exchange and correlation potential over the n$\mathbf{k}$ KS eigenvectors. The normalization factor $Z_{n\mathbf{k}}$ is defined as:

$$Z_{n\mathbf{k}} = \left[1 - \left\langle n\mathbf{k}\middle|\frac{\partial\Sigma(\omega)}{\partial\omega}\middle|n\mathbf{k}\right\rangle\Big|_{\omega=\epsilon_{n\mathbf{k}}}\right]^{-1} \qquad (2)$$

The expectation values of the self-energy are written as:

$$\Sigma_{nk} = -\int \frac{d\omega'}{2\pi i} e^{i\omega' 0^+} \left\langle \phi^{KS}_{n\mathbf{k}}\middle|G(\omega+\omega')W(\omega')\middle|\phi^{KS}_{n\mathbf{k}}\right\rangle . \quad (3)$$

The Green functions, G, are constructed using the DFT eigenfunctions, $\phi^{KS}_{n\mathbf{k}}$, and their corresponding eigenvalues, $\epsilon_{n\mathbf{k}}$. The dynamical screening effects in the self-energy, W, are treated within the generalized plasmon-pole model.[49] In the GW self-energy calculations, cutoff energies of 70 Ry and 12 Ry are applied for the exchange and correlation components, respectively, and up to 350 empty states are included in the summation over unoccupied states. A uniform k-point grid of 27 × 27 × 1 is utilized for both monolayers and bilayer heterostructures to ensure accurate BZ sampling. BZ sampling. To avoid numerical divergence of the coulomb potential at small $\mathbf{q}$ which creates convergence problems in the QP corrections of 2D semiconductors, we used the so-called Random Integration Method.[48]

Starting from the Kohn-Sham wave functions and the quasiparticle energies, the absorption spectra are calculated on the level of Bethe–Salpeter equation (BSE) formalism:[46,47,50,51]

$$\left(E_{c\mathbf{k}}-E_{v\mathbf{k}}\right)A^{S}_{vc\mathbf{k}}+\sum_{\mathbf{k}'v'c'}\left\langle vc\mathbf{k}\middle|K_{eh}\middle|v'c'\mathbf{k}'\right\rangle A^{S}_{v'c'\mathbf{k}'}=\Omega^{s}A^{S}_{vc\mathbf{k}} \tag{4}$$

where $A^{S}_{vc\mathbf{k}}$, Ω^{s}, and K_{eh} are the expansion coefficients of the excitons in electron-hole basis, the eigenenergies, and the kernel of the BSE, respectively .

Here, the excitonic Hamiltonian is constructed in the basis of electron-hole pairs, accounting for direct excitations at a given momentum $\mathbf{k}$ from a valence band state with quasiparticle energy $E_v(\mathbf{k})$ to a conduction band state with quasiparticle energy $E_c(\mathbf{k})$. The interaction kernel, K_{eh}, incorporates both the repulsive unscreened exchange interaction (V) and the attractive screened Coulomb interaction (W) between electron-hole states.These interactions can give rise to discrete excitonic states below the onset of the quasiparticle continuum. In the absence of electron-hole interactions i.e., when the interaction kernel K_{eh} is neglected, the optical excitations reduce to independent electron-hole pair transitions. In this case, the optical response of the system is governed by single-particle interband transitions without excitonic effects.

The optical absorption spectrum is given by the imaginary part of the dielectric function, $\epsilon(\omega)$, and can be calculated as

$$\epsilon(\omega)=1-\sum_{\mathbf{k}vc}\sum_{\mathbf{k}'v'c'}\lim_{\mathbf{q}\to 0}\frac{8\pi}{|\mathbf{q}|^{2}\Omega N_{q}}\rho^{*}_{vc\mathbf{k}}(\mathbf{q},\mathbf{G}) \times\rho_{v'c'\mathbf{k}'}(\mathbf{q}',\mathbf{G}')\sum_{\lambda}\frac{A^{\lambda}_{vc\mathbf{k}}(A^{\lambda}_{v'c'\mathbf{k}'})^{*}}{\omega-E_{\lambda}} \tag{5}$$

where ρ_{nm} are defined as[48]:

$$\rho_{nm}(\mathbf{k},\mathbf{q},\mathbf{G})=\langle n\mathbf{k}|e^{i(\mathbf{q}+\mathbf{G})\cdot\mathbf{r}}|m\mathbf{k}+\mathbf{q}\rangle\ . \tag{6}$$

The optical transitions are characterized by the dipole matrix elements, $\left\langle c\mathbf{k}\middle|p_i\middle|v\mathbf{k}\right\rangle$, which describe the coupling between valence and conduction states. The excitonic states are defined by their excitation energies, Ω^{s}, and corresponding amplitudes, A^{S}_{vck}. To achieve convergence in the solution of the Bethe-Salpeter equation (BSE), calculations were performed on the same k-point grid used in the GW calculations. The interaction kernel in the BSE was constructed using six conduction bands and six valence bands. A Lorentzian broadening of 0.15 eV was applied to simulate the absorption spectra. In both GW and BSE calculations, the Coulomb interaction was truncated to eliminate spurious interactions between periodic images of the layers.[52]

III. RESULTS AND DISCUSSION

A. Structural properties

WSe_2 and MoS_2 monolayers are transition-metal dichalcogenides (TMDs) made up of two Se (S) layers and hexagonal planes of W (Mo) atoms covalently bound to them in a trigonal prismatic coordination. Through vertical stacking of these two-dimensional crystals, a vdW structure is created, forming the heterobilayer WSe_2/MoS_2. Despite rotational alignment during fabrication, the small in-plane lattice mismatch (3-4 %) between WSe_2 and MoS_2, generates Moiré patterns.[22,53,54]

An atomic model of the R-type Moiré supercell is depicted in Figure 1(a), which follows the nomenclature of Ref.[22] (itself adapted from conventional stacking terminology[53,54]) and highlights three local energy-minimum configurations labeled AA, AB_W, and AB_{Se}. In Fig. 1(b), we show the atomic arrangements for these three local alignments. These arrangements correspond to the three stable energy-minimized states found in the heterobilayer, and the interaction between lattice mismatch and interlayer registry is reflected in the Moiré supercell geometry. Two local energy-maximum bridge configurations (Br and Br_2) are also accessible. These intermediate structures are produced through translation of the MoS_2 lattice with respect to WSe_2 between neighboring AB_{Se} sites. The arrangement of local atomic structures within these stacking configurations leads to a modification of interlayer forces, resulting in out-of-plane corrugations and spatially dependent distances between layers within the heterostructure.[22,53,54]

To model each labeled site in Fig. 1, a 1×1 WSe_2/MoS_2 heterobilayer unit cell was constructed, containing six atoms. The lattice constant was set to the average of the monolayer WSe_2 and MoS_2 lattice parameters, preserving the hexagonal symmetry inherent to the parent monolayers. The three stable stacking configurations examined here (AA, AB_W, and AB_{Se}) were predicted theoretically,[22] and observed experimentally in samples grown by chemical vapor deposition (CVD).[22,55] The AA stacking is constructed by positioning Mo atoms over W atoms and S atoms in one layer over Se atoms in the layer beneath with zero degree rotation of WSe_2 with respect to the MoS_2 layer. The difference in the local atomic registry between AA and AB stackings resides in the lateral alignment of the chalcogen atoms. AB_{Se} (AB_W) means that the hexagonal lattices of the metal atoms in the two monolayers are stacked in an AB manner with the Mo (W) atoms in the one layer are covered by chalcogen atoms in the other layer. In other words, W atoms is covered by S atoms in AB_{Se} and Mo atom is covered by Se atoms in AB_W. Consequently, interlayer coupling would be significantly influenced as we will see later in the paper.

According to the nomenclature of the previous study,[54] AA is an eclipsed stacking. The AB bernal stacking can be obtained by simple transformations from AA config-

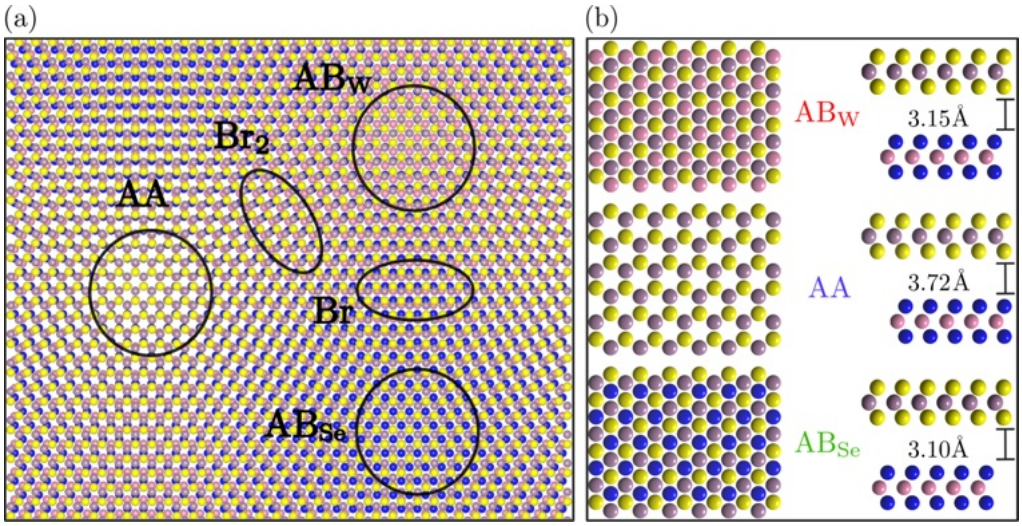

FIG. 1. (a) Schematic model of the Moiré pattern on an R-stacked WSe_2/MoS_2 heterobilayer. (b) Top and side views of the atomic models for AA, AB_W, and AB_{Se} registries zoomed in on a unit cell of the Moiré pattern.

uration by horizontal layer sliding. AB is staggered with metal atoms of one layer aligned with chalcogen atoms of the other layer and can be obtained by shifting the WSe_2 layer with respect to MoS_2 layers by $a/\sqrt{3}$, where a is the lattice parameter. Both AA and AB stacking orders are of R-type.

We computed the lattice constants, interlayer distances, and bond lengths for monolayers and bilayers. The lattice constant of the heterobilayer is approximately 3.23 Å, achieved through a 2.7 % in-plane compression of the monolayer WSe_2 and a 1.5 % expansion of the monolayer MoS_2 to enforce commensurability. In the three stacking configurations, the average Mo-S and W-Se bond lengths are 2.425 Å and 2.528 Å, respectively. These correspond to compressions of about 0.3 % (Mo-S) and 0.8 % (W-Se) relative to their isolated monolayer values. The minor deviations in lattice parameters and bond lengths from those of the parent monolayers are consistent with weak interlayer interactions. Our results align closely with prior theoretical and experimental studies.[22,56–59]

To evaluate the relative stability of the three configurations, we calculated their formation energies. Contributions from phonons were omitted due to the dominance of weak vdW interactions,[60] and zero-point vibrational effects were assumed negligible.[61] The AA stacking configuration exhibits a formation energy of -223 meV/cell, which is only 0.06 meV and 0.07 meV lower than those of AB_W and AB_{Se}, respectively. Although AA stacking is the most stable configuration, the very small energy differences between the three configurations indicate that they have comparable thermodynamic stability.

The interlayer distance d, which is the distance between the constituent layers [see Fig. 1(c)], is calculated to be approximately 3.72 Å, 3.15 Å, and 3.10 Å for AA, AB_W, and AB_{Se}, respectively. This distance is largest when the S atoms are directly aligned above the Se atoms, as this is the case in the AA registry. This occurs due to increased Pauli repulsion between the overlapping electron clouds localized around these atoms. On the contrary, in AB stacking configurations, the interlayer distance d is reduced due to the alignment of the metal atoms in one layer with the chalcogen atoms in the adjacent layer. This alignment strengthens the electrostatic attraction, resulting in a reduced separation between the Se and S atomic layers.

B. Electronic properties

Figure 2 shows the DFT and G_0W_0 band structures for monolayer WSe_2 and MoS_2, and their corresponding heterostructures. Consistent with prior studies,[26,42,58,62,63] both WSe_2 and MoS_2 monolayers exhibit direct band gap semiconducting behavior at their equilibrium geometries under DFT and G_0W_0 treatment [see Fig.2 (a)], a direct consequence of inversion symmetry breaking (group of symmetry D_{3h}) inherent to their honeycomb lattice structures.[4,7] Our mean field theory calculations reveal fundamental gaps of 1.62 eV (MoS_2) and 1.27 eV (WSe_2) at K point, with doubly degenerated valence bands predominantly of localized $d_{x^2-y^2}$ character. Spin-orbit (SO) coupling induces a splitting of the valence band into two uppermost valence bands (VB and VB-1), with energy separations of 457 meV in WSe_2 and 147 meV in MoS_2, consistent with prior theoretical and experimental reports.[42,58,59,64–67] Many-body G_0W_0 corrections substantially increase these fundamental gaps to 2.72 eV and 2.17 eV, respectively, showing excellent consistency with established theoretical references.[26,42,64,65,67,68] Discrepancies with values available in the literature likely

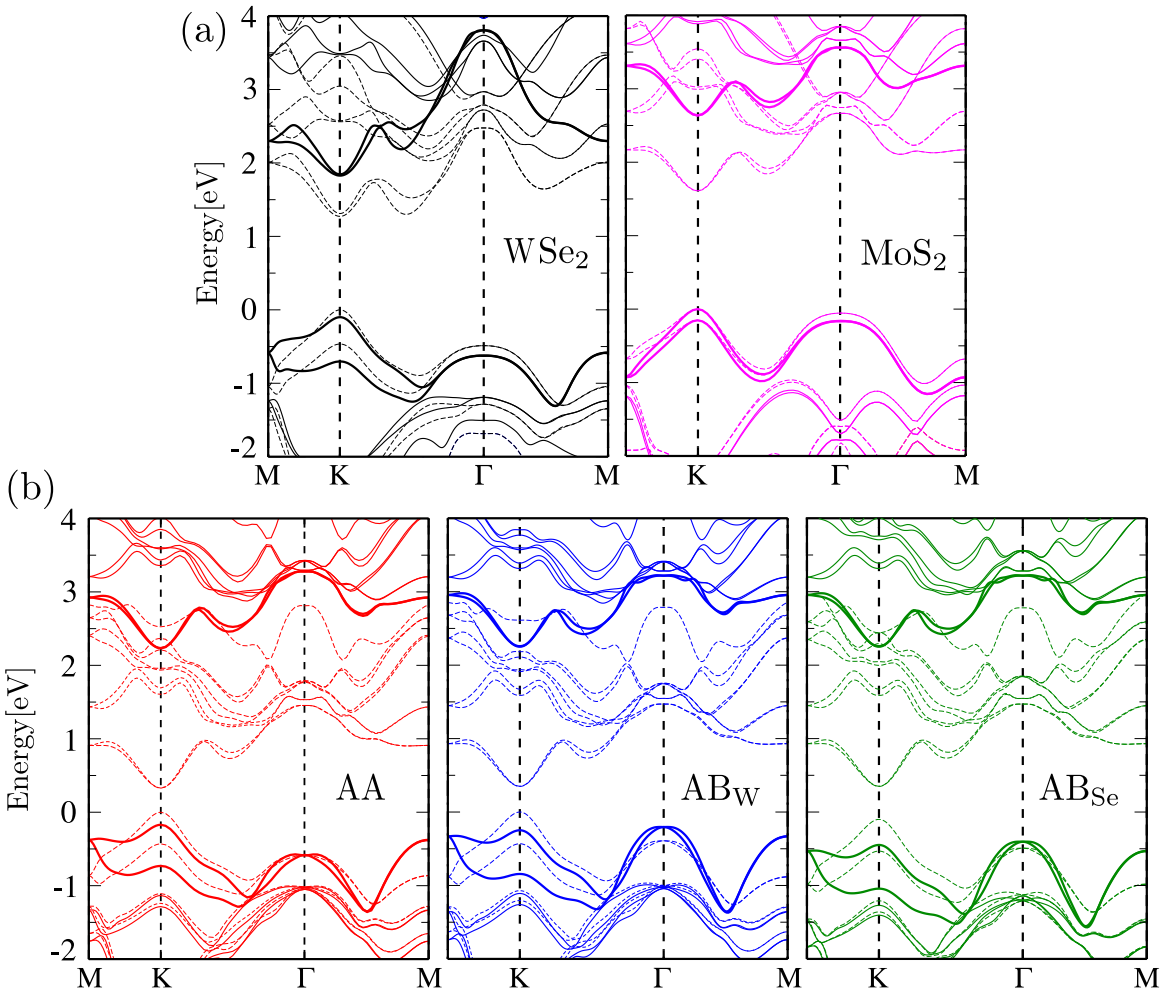

FIG. 2. (Color online) Band structures calculated DFT (GGA, thin dashed lines) and the G_0W_0 approximation (thick solid lines). Top panel: Monolayer MoS_2 (left) and monolayer WSe_2 (right). From left to right in the bottom panel: AA, AB_W, and AB_{Se} stacked WSe_2/MoS_2 heterobilayers.

originate from variations in computational parameters, particularly exchange-correlation functional implementations and unit cell optimizations.

For heterobilayers [Fig. 2(b)], DFT calculations reveal direct band gaps at the K point, with twofold degenerate valence band. The computed band gaps are 0.33 eV (AA), 0.35 eV (AB_W), and 0.45 eV (AB_{Se}), in agreement with existing literature.[65,66] Crucially, the bandgap tunability with stacking order suggests a pathway to tailor electronic properties via layer arrangement. Near the K-point, hybridization effects dominate the band edges, driven by the d orbital contributions of the metal atoms: the valence band arises from hybridization of W $5d_{x^2-y^2}$ and $5d_{3z^2-r^2}$ orbitals, while the conduction band is predominantly derived from Mo $4d_{3z^2-r^2}$ orbitals. To model the local configurations, we employed 1×1 WSe_2/MoS_2 unit cells with a fixed in-plane lattice constant of 3.23 Å, corresponding to the average of the unstrained monolayer lattice parameters. In this configuration, the MoS_2 layer experiences tensile strain, while the WSe_2 layer is under compressive strain. Although the influence of this strain on the interlayer interactions is expected to be minor, we assessed its effect by comparing the electronic band structures of unstrained and strained monolayers. Our calculations indicate that the band gap of monolayer WSe_2 increases by approximately 3 %, while the band gap of monolayer MoS_2 decreases by about 7 %.

Interlayer vdW interactions in WSe_2/MoS_2 heterobilayers yield a type-II band alignment, wherein the valence band and the conduction band are localized on distinct monolayers. This spatial separation of charge carriers generates momentum-direct charge-transfer excitons, with holes confined to WSe_2 and electrons to MoS_2. Such a mechanism profoundly influences optical properties and presents compelling opportunities for optoelectronic applications, including excitonic devices and light-harvesting systems. At the DFT level, heterobilayer band gaps are typically smaller than those of the individual monolayers due to interlayer interactions and orbital hybridization between the two layers. Specifically,

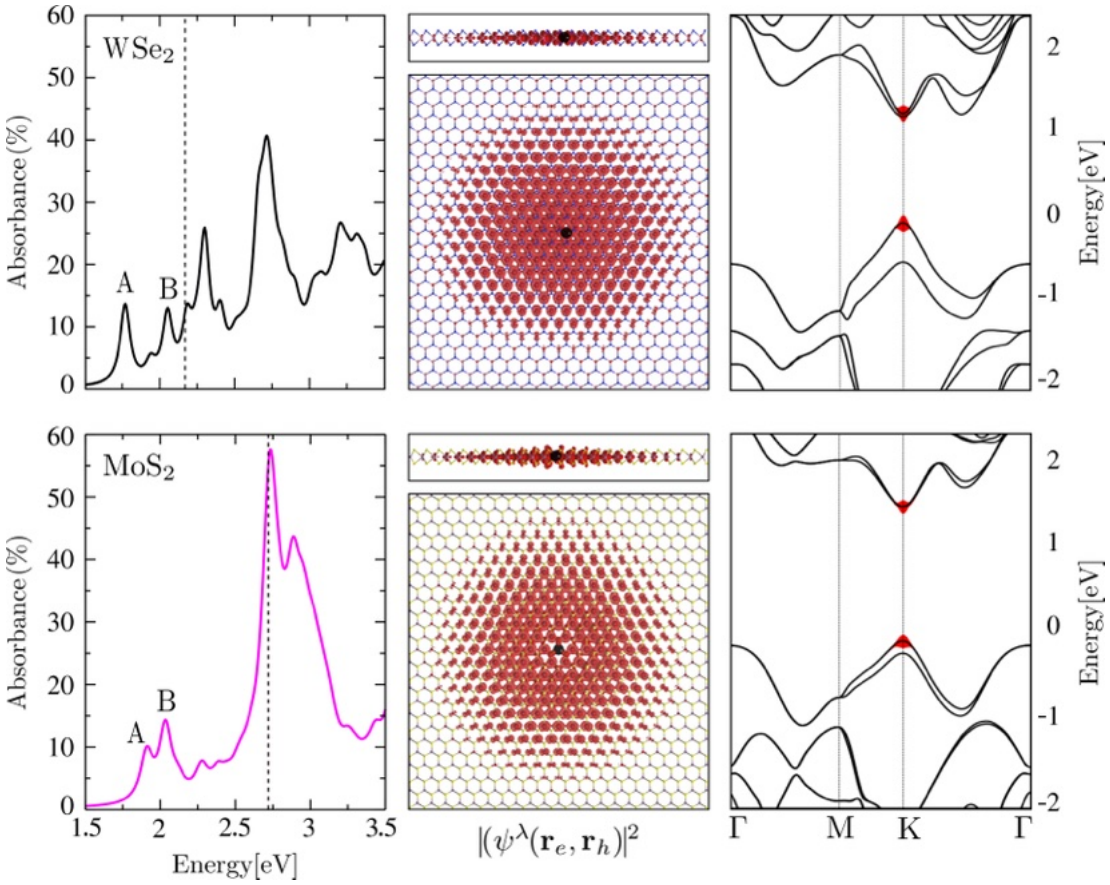

FIG. 3. (Color online) Left: Optical absorption spectra of WSe_2 and MoS_2 single layers, given by the absorbance. QP band gaps are marked with vertical dashed lines, and the labels indicate the peaks associated with the A and B excitons. Middle: Side view and top view of exciton A charge density. Right: Reciprocal-space distribution of the exciton A. The sizes of the red patches are indicative of the weights of the involved QP states.

the $d_{3z^2-r^2}$ orbitals of W and Mo atoms overlap across the layers, modifying the band structure through interlayer coupling. These d orbitals are more localized than s and p orbitals and often exhibit strong electron-electron repulsion, leading to huge electronic correlation effects. Standard DFT, especially with local or semi-local functionals such as GGA, often struggles to capture these correlation effects accurately, particularly for the localized d electrons. Consequently, DFT may not account for the strong Coulomb interactions within the d orbitals, which reduces the energy difference between the valence $5d$ bands and the conduction $4d$ bands, thereby leading to a smaller fundamental band gap in the bilayer system compared to the parent monolayers.

Moreover, accounting for electron-electron interactions through a G_0W_0 calculation significantly enhances the band gap by over 80%. This result aligns closely with prior theoretical studies.[65] Interestingly, the AA stacking configuration retains its direct band gap character at K, while AB stackings transition to indirect band gap materials upon the inclusion of electron-electron self-energy. The origin of this difference is the interlayer interaction. While the CB remains at the K point, the VB shifts from K to Γ. This shift can explained by the differences in the effective mass of the charge carriers at these hight-symmetry points. The electron-electron interactions modify the effective mass, which affects the energy dispersion near the band edges. In AB stacking configurations, the effective mass at the Γ point would be lighter compared to K point making it energetically favorable for the VB to relocate, resulting in an indirect band gap in the AB stacking configuration. The AA registry is predicted to exhibit a direct band gap of 2.40 eV, highlighting its potential for optoelectronic applications due to its suitability as an efficient light emitter. For AB_W and AB_{Se} registries, direct band gaps of 2.50 eV and 2.70 eV are observed at the K-point, while indirect gaps of 2.44 eV and 2.65 eV are found between the Γ and K points. The small difference between the direct and indirect band gaps suggests that these materials may also be promising for optoelectronic applications, as they remain effective light emitters. The large quasiparticle corrections to the PBE band gap originates from the enhancement of the electron-electron interaction and the weakening of the screening response in two-dimensional materials. Such a low screening gives rise to bound ex-

citons with large binding energies. The bilayers possess the factor group C_{3v}, which also lacks inversion symmetry. This lack of symmetry, combined with SO coupling, result in valence band splitting. The values are 562 meV, 594 meV, and 600 meV for AA, AB_W, and AB_{Se}, respectively, demonstrating a marked enhancement compared to monolayer counterparts. This increased splitting may arise from interlayer coupling, which introduces an additional contribution to the SO interaction beyond monolayer effects.

C. Optical absorption spectra

In figure 3 are shown the optical absorption spectra of monolayer WSe_2 (top left panel) and MoS_2 (bottom left panel), revealing striking similarities in their low-energy excitonic features. All systems exhibit a characteristic double-peak structure at the absorption onset (denoted as A and B excitons). These spectral features come from strong interactions between electrons that create tightly bound excitons, which mainly influence how the material responds to light. The energy splitting between A and B excitons reflects spin-orbit coupling (SOC) effects in the valence band. Monolayer MoS_2 exhibits a splitting of 114 meV, while WSe_2 shows a larger splitting of 183 meV, attributed to the heavier tungsten atom enhancing SOC. The A (B) exciton is found at 1.76 eV (1.93 eV) and 1.91 eV (2.03 eV) in MoS_2 and WSe_2 monolayers, respectively, with binding energies of 0.81 eV (A) and 0.61 eV (B) for MoS_2, and 0.40 eV (A) and 0.23 eV (B) for WSe_2, which values significantly exceeding those in bulk semiconductors. Our results are in good agreement with previous calculations[62,69] and experiments.[70] This enhancement stems from reduced dielectric screening in atomically thin layers, which amplifies Coulomb interactions.

The lowest-energy exciton is optically forbidden in these structures, despite broken inversion symmetry. While the presence or absence of inversion symmetry in a crystal fundamentally dictates the optical activity of excitonic states, additional factors such as spin-orbit coupling (SOC) and band-edge orbital symmetries determine whether the lowest-energy exciton is optically active (bright) or inactive (dark). This distinction becomes apparent when comparing the excitonic behavior of these monolayers with that of hexagonal boron nitride (hBN),[71] despite both of which crystallize in the non-centrosymmetric D_{3h} point group. In hBN, the weak SOC and $\pi \rightarrow \pi^*$ character of the band edges ensure that the lowest exciton remains bright, as the dipole-allowed transition is symmetry-permitted. In contrast, monolayer WSe_2 and MoS_2 exhibit strong SOC, which lifts the spin degeneracy of both valence and conduction bands, giving rise to a spin-forbidden exciton that can lie below the bright A exciton in energy. Despite the lack of inversion symmetry, which typically permits dipole transitions, the excitonic ground state in monolayer WSe_2 and MoS_2 can therefore be dark. These observations drive home that, while inversion symmetry sets the general optical selection rules, the fine structure of excitonic states and the relative ordering of bright and dark excitons depend sensitively on SOC strength, orbital hybridization, and symmetry of the band edges.

In the middle panel of Fig. 3, we plot the squared magnitude of the real-space wave function for the exciton corresponding to peak A in monolayer WSe_2 and MoS_2, with the hole localized near a W atom in WSe_2 and a Mo atom in MoS_2. The spatial profile of this exciton exhibits a nearly circular symmetry, closely resembling the $1s$ orbital of a 2D hydrogenic system. In both monolayers, the electron density for the exciton in both materials predominantly localizes on nearest-neighbor metallic atoms adjacent to the hole, reflecting restricted spatial charge separation. This pronounced overlap between electron and hole wave functions indicates shorter excitonic radiative lifetimes. The electron density profiles exhibit rapid spatial decay, characteristic of tightly bound electron-hole $(e-h)$ pairs. Notably, the exciton MoS_2 displays a more localized charge distribution compared to its counterpart in WSe_2, consistent with its highest binding energy. This trend indicates a direct correlation between binding energy and spatial delocalization: reduced binding energy corresponds to progressively extended excitonic wave functions.

As illustrated in the right panel of Fig. 3, this exciton originates from electronic transitions involving the in-plane $d_{z^2-r^2}$ orbital in the VB band and the out-of-plane d_{z^2} orbital in the CB of the metal atoms. It is important to note that the real-space wave function of exciton B is spatially indistinguishable from that of exciton A. This equivalence arises from the conservation of spin as a good quantum number at the K and K' valleys.[18] Despite spin-orbit-induced splitting in the valence bands, the spatial components of the valence band wave functions remain identical across both valleys. Consequently, peaks A and B, which stem from transitions between the spin-orbit-split valence bands (VB, VB-1) and the lowest conduction band (CB) at the K and K' valleys, respectively, share identical spatial wave functions. Although these excitons originate from distinct valleys and exhibit different spin configurations, their spatial structures are invariant under spin conservation, reflecting the symmetry imposed by valley-dependent spin selection rules.

Beyond the A and B peaks, the absorption spectrum contains contributions from weakly bound electron-hole pairs. At higher energies, the absorption increases abruptly, being in accordance with direct band-to-band transitions, where excitonic effects become negligible. Subtle variations in peak shapes and spectrum breadth across materials arise from differences in carrier effective masses, SOC strength, and dielectric screening mechanisms. Our findings exhibit excellent agreement with prior experimental and theoretical studies,[25,26,63,67] validating the robustness of the observed trends.

We now turn to the excitonic properties of heterobi-

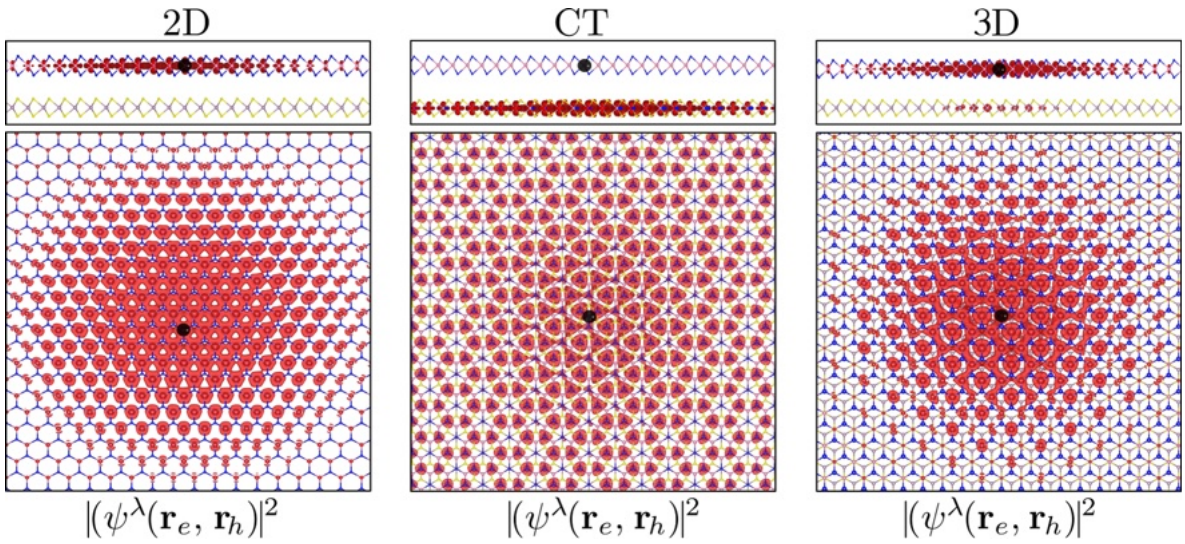

FIG. 4. (Color online) Side view and top view of exciton of charge densities (side and top view) of the three types of excitons that can emerge in WSe_2/MoS_2 heterobilayer upon different stacking configurations. From left to right: a 2D exciton, where the electron and hole reside within the same layer; a charge-transfer (CT) exciton, with the electron and hole pinned in different layers, and 3D exciton where the hole is located in one layer while the electron is distributed across both layers. The hole is indicated by a black dot, while the electron distribution is depicted by the red isosurface.

layers. In Fig. 4, we display the real-space distributions of three exciton types found in different stacking configuration. The first type is a 2D exciton, with the electron and the hole settle in the same layer. These excitons can be further classified into MoS_2-like exciton (2D-MoS_2) and WSe_2-like exciton (2D-WSe_2) states in the in-plane direction. The second type is the charge transfer (CT) excitons, where the electron and the hole sit on different layers. The third category is the three-dimensional (3D) exciton, where the hole is confined to one layer while the electron is distributed across both layers.

In all cases, the excitonic wave functions exhibit trigonal symmetry, which mirrors the hexagonal lattice symmetry of the monolayer. Moreover, their charge distributions display extended features, indicative of localization in reciprocal space [see Fig. 5]. The stacking-dependent structural and electronic properties are reflected in different optical responses. Specifically, the AA and AB_{Se} stacking arrangements accommodate the three exciton types, whereas the AB_W configuration supports only 2D and CT excitons. These excitonic characteristics are intimately linked to the symmetry and atomic registry of each stacking arrangement. To explain these features, we analyze the electronic band structures and optical spectra, emphasizing their interplay with the underlying atomic geometry.

In the eclipsed AA stacking, all atoms in the two nonequivalent layers align perfectly, with Mo atoms positioned directly above W atoms and S atoms directly above Se atoms. In contrast, the AB staggered stacking adopts a hollow-site registry, wherein alternating atoms occupy hollow sites. Specifically, in the AB_{Se} stacking, Mo and Se atoms are located at hollow positions, whereas in AB_W, W and S atoms occupy these sites [see Fig. 1(b)]. These different lateral registries result in varying electronic structures [see Fig. 2(b)], which in turn influence the optical spectra [see Fig. 5]. In the following discussion, we examine how these structural properties govern the formation of various $e-h$ pairs.

In Fig. 5 we display the optical spectra (left panel) together with the band structures (right panel) [see also Fig. S1 in the Supplemental Material[72]]. Our calculations reveal a significant redistribution of oscillator strength accompanied by a pronounced redshift of the absorption spectrum. Notably, we observe the emergence of strong excitonic resonances below the single-particle continuum onset, along with a large manifold of optically forbidden excitonic states below the onset of single-particle transition continuum

First, we begin by examining the 2D exciton depicted in Fig. 4 [see also Fig. S2 left panel in the Supplemental Material[72]]. This bound electron-hole ($e-h$) pair is observed across all three stacking arrangements, manifesting as the first bright excitons in each registry. In the AA configuration, it is non-degenerate and emerges at an energy of 2.17 eV, with a binding energy of 0.23 meV. Similar to the A exciton in monolayers, its wave function envelope is nearly azimuthally symmetric. This exciton marked in the spectrum of Fig. 5 arises from transitions between the VB and the CB+3 states near the band extrema at the high-symmetry K point, as shown in Fig. 5 (right panel). Since both the VB and the CB+3 originate from orbitals localized in the W-based monolayer, hole localization within this layer confines the electronic charge density to the same layer, confirming its 2D character (2D-WSe_2). In AB stacking configuration, this exciton

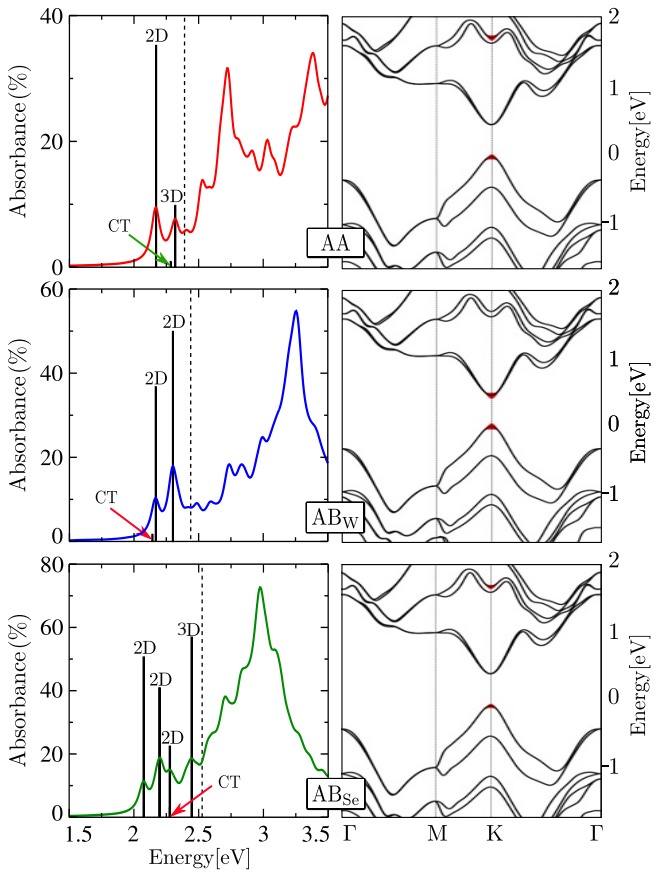

FIG. 5. (Color online) Left: Optical absorption spectra, given by the absorbance in AA, AB_W and AB_{Se} registries. The dashed line indicates the direct QP gap. Right: Band (DFT) contributions to the excitations marked in the spectra following the nomenclature in Fig. 4. The sizes of the red patches are indicative of the weights of the involved states. The 2D exciton of AA stacking exhibits WSe_2-like character, whereas those of the AB stacking are of MoS_2-like.

is on MoS_2 layer (2D-MoS_2), and due to the symmetry of the lattice it exhibits a twofold degeneracy. In the AB_{Se} configuration, it emerges at 2.07 eV with a notably high binding energy of 0.58 eV, while in the AB_W configuration, it appears at 2.16 eV with a binding energy of 0.27 eV. In both cases, these excitons arise from transitions between the VB-2 and CB/CB+1 states at the K point. Notice that the electron density associated with the 2D exciton is primarily localized on the nearest-neighbor metal atoms adjacent to the hole, resulting in restricted spatial charge separation and, consequently, reduced excitonic radiative lifetimes.

Next, we examine the CT excitons, also depicted in Fig. 4. These doubly degenerate optically forbidden excitons are also found in all stacking configurations, appearing as the first exciton in all registries. In AA, the CT exciton marked in the spectrum of Fig. 4 emerges at about 2.28 eV. It is twofold degenerate, with a binding energy of 0.23 eV, and originates from interband transitions between the valence and conduction bands at the high-symmetry K point. In the spectrum of AB_W configuration, the CT exciton observed at 2.16 eV, has a binding energy of 0.28 eV, and arises from transitions between the VB and CB near K point. In the AB_{Se} arrangement, the CT exciton located at 2.27 eV has a binding energy of 0.38 eV. It originates from transitions between the VB and the CB/CB+1, and between the VB and the CB, at the K point. Here, the hole is localized on the W$dz^2 - y^2$ orbitals and the corresponding electronic wave functions are spread over metallic atoms belonging to MoS_2 layer. Further details are provided in the Supplemental Material.[72]

The final exciton type, 3D, is found exclusively in AA and AB_{Se} stacking configurations, appearing as the second bright exciton. It is a doubly degenerate exciton and appears at 2.32 eV with a binding energy of 0.08 eV, stemming from transitions between the VB and CB+4 states at the high-symmetry K point. This wave function of this exciton is delocalized over the whole space and displaying extended features. In AB_{Se}, the equivalent exciton appears at 2.44 eV with a binding energy of 0.21 eV. It is also degenerate and originates from transitions between the VB and CB+4 states in the vicinity of the K point. Interestingly, this bright exciton demonstrates pronounced localization, extending over just a few lattice constants. Interestingly, we observe a characteristic dumbbell-like distribution of electron density around each W atom in all exciton types. This feature arises from the d orbitals of individual metallic atoms and persists across all stacking configurations [see Fig. 5 and Fig. S2 in the Supplemental Material[72]].

The absence of 3D excitons in the AB_W stacking configuration is due to a complex interplay of symmetry constraints, interlayer hybridization effects, and orbital-specific interactions. In the AB_W registry, where W and S atoms occupy hollow sites, the resulting potential landscape and orbital overlap differ fundamentally from the AB_{Se} case. The 3D excitons observed in AA and AB_{Se} stackings originate from transitions to highly delocalized CB+4 states that require strong interlayer hybridization of Mo-d and W-d orbitals, a condition that is apparently not satisfied in AB_W due to the more localized nature of W-derived states near the Fermi level. This localization originates from both the stronger d-orbital confinement of W atoms and the particular nodal structure of the electronic wavefunctions in AB_W, which restricts charge delocalization across the heterobilayer. Furthermore, the AB_W band structure exhibits significant renormalization of higher conduction bands, with CB+4 states either shifting outside the relevant energy window or becoming optically forbidden due to registry-dependent selection rules. This difference with the AB_{Se} stacking configuration highlights how variations in the atomic registry can dramatically modify the dimensionality of excitonic states. The absence of 3D excitons in AB_W clearly shows how stacking symmetry can be an effective way to control

excitons in van der Waals heterostructures.

IV. CONCLUSION

To summarize, we have systematically investigated the excitonic landscape in single-layer WSe_2/MoS_2 heterojunctions, focusing on the role of different stacking configurations. On the one hand, our analysis reveals that tightly bound excitons with an interlayer 3D character are uniquely present in the AA and AB_{Se} stackings, where the atomic registry enables strong out-of-plane hybridization via transition-metal d-orbitals (Mo/W) coupling. On the other hand, 2D excitons and interlayer charge-transfer excitons can be found in all stacking types, showing that in-plane quantum confinement and interlayer dipole coupling are strong regardless of differences in symmetry. These findings highlight the delicate interplay between structural arrangement and excitonic properties, providing key tools for engineering van der Waals heterostructures with tailored electronic and optical responses.

The flat and commensurate stacking configurations examined in the present study occur within real materials, as observed in transition metal dichalcogenides (TMDs) and their vdW heterostructures.[22,73–75] As a consequence, our results offer important insights into the electronic and optical properties of such microscopic regions, which can significantly influence the behavior of the overall system. This is particularly relevant in the context of Moiré crystals, which are distinguished by their complex interlayer arrangements and rotational alignments, as reported in TMD-based vdW heterojunctions.[22,73–90] Our results contribute to a deeper understanding of fundamental structure-property relationships at the cutting edge of ab initio many-body theory, building on recent advances in the study of TMD-based vdW heterostructures and their emergent phenomena.[77] Despite the fact that these advanced computational methods are often challenging for modeling superlattices with realistic unit cell sizes due to their substantial computational demands, they provide us with essential basic data for constructing model Hamiltonians and semiempirical approaches capable of addressing these complex systems, as highlighted in recent studies on TMD-based vdW heterostructures.[91–96] These insights are crucial for advancing the design and understanding of next-generation quantum materials and devices based on TMD vdW heterostructures heterostructures.[33]

V. ACKNOWLEDGMENTS

This work has been been supported by the open research fund of the General Direction of Research and Technological Development (DGRSDT) of the Ministry of Higher Education and Scientific Research, Algeria and by the Deutsche Forschungsgemeinschaft (DFG, German Research Foundation) through the research unit QUAST, FOR 5249 P7 ID No. 449872909. Ab initio simulations were performed using computational resources from the HPC facility at the University of Batna 2 (Algeria), local clusters from CNR ISM at Monterotondo (Italy), and the Head1 ITP cluster at Heidelberg University (Germany) under scholarship Coimbra 2024. W.L and K.R thank Dr Andrea Marini for his outstanding help and valuable advice, W.L acknowledges Dr. Fulvio Paleari for technical assistance with the Yambo code and Yambopy toolkit .

[1] K. S. Novoselov, A. Mishchenko, A. Carvalho, and A. H. C. Neto, Science **353**, aac9439 (2016), https://www.science.org/doi/pdf/10.1126/science.aac9439.
[2] F. Xia, H. Wang, D. Xiao, M. Dubey, and A. Ramasubramaniam, "Two-dimensional material nanophotonics," (2014).
[3] H. Fang, S. Chuang, T. C. Chang, K. Takei, T. Takahashi, and A. Javey, Nano Letters **12**, 3788 (2012), pMID: 22697053, https://doi.org/10.1021/nl301702r.
[4] K. F. Mak, C. Lee, J. Hone, J. Shan, and T. F. Heinz, Phys. Rev. Lett. **105**, 136805 (2010).
[5] K. F. Mak and J. Shan, Nature Photonics **10**, 216 (2016).
[6] Q. H. Wang, K. Kalantar-Zadeh, A. Kis, J. N. Coleman, and M. S. Strano, Nature Nanotechnology **7**, 699 (2012).
[7] A. Splendiani, L. Sun, Y. Zhang, T. Li, J. Kim, C.-Y. Chim, G. Galli, and F. Wang, Nano Letters **10**, 1271 (2010), pMID: 20229981, https://doi.org/10.1021/nl903868w.
[8] O. Lopez-Sanchez, D. Lembke, M. Kayci, A. Radenovic, and A. Kis, Nature Nanotechnology **8**, 497 (2013).
[9] F. H. L. Koppens, T. Mueller, P. Avouris, A. C. Ferrari, M. S. Vitiello, and M. Polini, Nature Nanotechnology **9**, 780 (2014).
[10] J. S. Ross, P. Klement, A. M. Jones, N. J. Ghimire, J. Yan, D. G. Mandrus, T. Taniguchi, K. Watanabe, K. Kitamura, W. Yao, D. H. Cobden, and X. Xu, Nature Nanotechnology **9**, 268 (2014).
[11] A. Pospischil, M. M. Furchi, and T. Mueller, Nature Nanotechnology **9**, 257 (2014).
[12] B. W. H. Baugher, H. O. H. Churchill, Y. Yang, and P. Jarillo-Herrero, Nature Nanotechnology **9**, 262 (2014).
[13] M. Bernardi, M. Palummo, and J. C. Grossman, Nano Letters **13**, 3664 (2013), pMID: 23750910, https://doi.org/10.1021/nl401544y.
[14] M. M. Furchi, A. Pospischil, F. Libisch, J. Burgdörfer, and T. Mueller, Nano Letters **14**, 4785 (2014), pMID: 25057817, https://doi.org/10.1021/nl501962c.
[15] G. Wang, A. Chernikov, M. M. Glazov, T. F. Heinz, X. Marie, T. Amand, and B. Urbaszek, Rev. Mod. Phys. **90**, 021001 (2018).
[16] T. Cao, G. Wang, W. Han, H. Ye, C. Zhu, J. Shi, Q. Niu, P. Tan, E. Wang, B. Liu, and J. Feng, Nature Communications **3**, 887 (2012).

[17] X. Xu, W. Yao, D. Xiao, and T. F. Heinz, Nature Physics **10**, 343 (2014).
[18] D. Xiao, G.-B. Liu, W. Feng, X. Xu, and W. Yao, Phys. Rev. Lett. **108**, 196802 (2012).
[19] K. F. Mak, K. L. McGill, J. Park, and P. L. McEuen, Science **344**, 1489 (2014), https://www.science.org/doi/pdf/10.1126/science.1250140.
[20] A. Kormányos, G. Burkard, M. Gmitra, J. Fabian, V. Zólyomi, N. D. Drummond, and V. Fal'ko, 2D Materials **2**, 022001 (2015).
[21] A. K. Geim and I. V. Grigorieva, Nature **499**, 419 (2013).
[22] C. Zhang, C.-P. Chuu, X. Ren, M.-Y. Li, L.-J. Li, C. Jin, M.-Y. Chou, and C.-K. Shih, Science Advances **3**, e1601459 (2017), https://www.science.org/doi/pdf/10.1126/sciadv.1601459.
[23] C.-H. Lee, G.-H. Lee, A. M. van der Zande, W. Chen, Y. Li, M. Han, X. Cui, G. Arefe, C. Nuckolls, T. F. Heinz, J. Guo, J. Hone, and P. Kim, Nature Nanotechnology **9**, 676 (2014).
[24] Y. Yu, Y. Yu, C. Xu, A. Barrette, K. Gundogdu, and L. Cao, Phys. Rev. B **93**, 201111 (2016).
[25] M. Palummo, M. Bernardi, and J. C. Grossman, Nano Letters **15**, 2794 (2015).
[26] A. Molina-Sánchez, D. Sangalli, K. Hummer, A. Marini, and L. Wirtz, Phys. Rev. B **88**, 045412 (2013).
[27] Y. Gong, J. Lin, X. Wang, G. Shi, S. Lei, Z. Lin, X. Zou, G. Ye, R. Vajtai, B. I. Yakobson, H. Terrones, M. Terrones, B. Tay, J. Lou, S. T. Pantelides, Z. Liu, W. Zhou, and P. M. Ajayan, Nature Materials **13**, 1135 (2014).
[28] L. Britnell, R. M. Ribeiro, A. Eckmann, R. Jalil, B. D. Belle, A. Mishchenko, Y.-J. Kim, R. V. Gorbachev, T. Georgiou, S. V. Morozov, A. N. Grigorenko, A. K. Geim, C. Casiraghi, A. H. C. Neto, and K. S. Novoselov, Science **340**, 1311 (2013), https://www.science.org/doi/pdf/10.1126/science.1235547.
[29] W. Aggoune, C. Cocchi, D. Nabok, K. Rezouali, M. Akli Belkhir, and C. Draxl, The Journal of Physical Chemistry Letters **8**, 1464 (2017), pMID: 28296404, https://doi.org/10.1021/acs.jpclett.7b00357.
[30] E. C. Regan, D. Wang, C. Jin, M. I. Bakti Utama, B. Gao, X. Wei, S. Zhao, W. Zhao, Z. Zhang, K. Yumigeta, M. Blei, J. D. Carlström, K. Watanabe, T. Taniguchi, S. Tongay, M. Crommie, A. Zettl, and F. Wang, Nature **579**, 359 (2020).
[31] Y. Tang, L. Li, T. Li, Y. Xu, S. Liu, K. Barmak, K. Watanabe, T. Taniguchi, A. H. MacDonald, J. Shan, and K. F. Mak, Nature **579**, 353 (2020).
[32] L. Britnell, R. V. Gorbachev, R. Jalil, B. D. Belle, F. Schedin, A. Mishchenko, T. Georgiou, M. I. Katsnelson, L. Eaves, S. V. Morozov, N. M. R. Peres, J. Leist, A. K. Geim, K. S. Novoselov, and L. A. Ponomarenko, Science **335**, 947 (2012), https://www.science.org/doi/pdf/10.1126/science.1218461.
[33] F. Withers, O. Del Pozo-Zamudio, A. Mishchenko, A. P. Rooney, A. Gholinia, K. Watanabe, T. Taniguchi, S. J. Haigh, A. K. Geim, A. I. Tartakovskii, and K. S. Novoselov, Nature Materials **14**, 301 (2015).
[34] P. Hohenberg and W. Kohn, Phys. Rev. **136**, B864 (1964).
[35] W. Kohn and L. J. Sham, Phys. Rev. **140**, A1133 (1965).
[36] P. Giannozzi, S. Baroni, N. Bonini, M. Calandra, R. Car, C. Cavazzoni, D. Ceresoli, G. L. Chiarotti, M. Cococcioni, I. Dabo, *et al.*, Journal of physics: Condensed matter **21**, 395502 (2009).
[37] A. Marini, C. Hogan, M. Grüning, and D. Varsano, Computer Physics Communications **180**, 1392 (2009).
[38] D. Sangalli, A. Ferretti, H. Miranda, C. Attaccalite, I. Marri, E. Cannuccia, P. Melo, M. Marsili, F. Paleari, A. Marrazzo, G. Prandini, P. Bonfà, M. O. Atambo, F. Affinito, M. Palummo, A. Molina-Sánchez, C. Hogan, M. Grüning, D. Varsano, and A. Marini, Journal of Physics: Condensed Matter **31**, 325902 (2019).
[39] D. R. Hamann, Phys. Rev. B **88**, 085117 (2013).
[40] J. P. Perdew, K. Burke, and M. Ernzerhof, Phys. Rev. Lett. **77**, 3865 (1996).
[41] S. Grimme, J. Antony, S. Ehrlich, and H. Krieg, The Journal of Chemical Physics **132**, 154104 (2010).
[42] T. Cheiwchanchamnangij and W. R. L. Lambrecht, Phys. Rev. B **85**, 205302 (2012).
[43] H. J. Monkhorst and J. D. Pack, Phys. Rev. B **13**, 5188 (1976).
[44] L. Hedin, Phys. Rev. **139**, A796 (1965).
[45] M. S. Hybertsen and S. G. Louie, Phys. Rev. Lett. **55**, 1418 (1985).
[46] M. Rohlfing and S. G. Louie, Phys. Rev. B **62**, 4927 (2000).
[47] G. Onida, L. Reining, and A. Rubio, Rev. Mod. Phys. **74**, 601 (2002).
[48] A. Guandalini, P. D'Amico, A. Ferretti, and D. Varsano, npj Computational Materials **9**, 44 (2023).
[49] R. W. Godby and R. Needs, Physical review letters **62**, 1169 (1989).
[50] W. Hanke and L. J. Sham, Phys. Rev. B **21**, 4656 (1980).
[51] G. Strinati, La Rivista del Nuovo Cimento (1978-1999) **11**, 1826 (1988).
[52] C. A. Rozzi, D. Varsano, A. Marini, E. K. U. Gross, and A. Rubio, Phys. Rev. B **73**, 205119 (2006).
[53] J. D. Bernal, Proc. R. Soc. London, Ser. A **106**, 749 (1924).
[54] G. Constantinescu, A. Kuc, and T. Heine, Phys. Rev. Lett. **111**, 036104 (2013).
[55] Y.-C. Lin, R. Ghosh, Ram Krishna nad Addou, N. Lu, S. M. Eichfeld, H. Zhu, M.-Y. Li, X. Peng, M. J. Kim, L.-J. Li, R. M. Wallace, S. Datta, and J. A. Robinson, Nature Communications **6**, 7311 (2015).
[56] Y. Ding, Y. Wang, J. Ni, L. Shi, S. Shi, and W. Tang, Physica B: Condensed Matter **406**, 2254 (2011).
[57] C.-H. Chang, X. Fan, S.-H. Lin, and J.-L. Kuo, Phys. Rev. B **88**, 195420 (2013).
[58] A. Ramasubramaniam, Phys. Rev. B **86**, 115409 (2012).
[59] D. Le, A. Barinov, E. Preciado, M. Isarraraz, I. Tanabe, T. Komesu, C. Troha, L. Bartels, T. S. Rahman, and P. A. Dowben, Journal of Physics: Condensed Matter **27**, 182201 (2015).
[60] G. J. Slotman, G. A. de Wijs, A. Fasolino, and M. I. Katsnelson, Annalen der Physik **526**, 381 (2014).
[61] M. Milko, P. Puschnig, and C. Draxl, Phys. Rev. B **86**, 155416 (2012).
[62] N. Dadkhah and W. R. L. Lambrecht, Phys. Rev. B **109**, 195155 (2024).
[63] D. Y. Qiu, F. H. da Jornada, and S. G. Louie, Phys. Rev. Lett. **111**, 216805 (2013).
[64] D. Y. Qiu, F. H. da Jornada, and S. G. Louie, Phys. Rev. Lett. **111**, 216805 (2013).
[65] K. Dange, R. Yogi, and A. Shukla, Phys. Rev. Appl. **23**, 014008 (2025).
[66] H. Terrones, F. López-Urías, and M. Terrones, Scientific Reports **3**, 1549 (2013).
[67] Y.-C. Shih, F. A. Nilsson, and G.-Y. Guo, Phys. Rev. B **110**, 205417 (2024).

[68] E. S. Kadantsev and P. Hawrylak, Solid State Communications **152**, 909 (2012).

[69] M. Marsili, A. Molina-Sánchez, M. Palummo, D. Sangalli, and A. Marini, Phys. Rev. B **103**, 155152 (2021).

[70] R. Schmidt, I. Niehues, R. Schneider, M. Drüppel, T. Deilmann, M. Rohlfing, S. M. de Vasconcellos, A. Castellanos-Gomez, and R. Bratschitsch, 2D Materials **3**, 021011 (2016).

[71] W. Aggoune, C. Cocchi, D. Nabok, K. Rezouali, M. A. Belkhir, and C. Draxl, Phys. Rev. B **97**, 241114 (2018).

[72] See Supplemental Material at [ ] for additional results, including RPA and BSE optical absorption spectra, exciton charge density distributions, and exciton weights projected onto the interpolated band structure..

[73] J. H. Yu, H. R. Lee, S. S. Hong, D. Kong, H.-W. Lee, H. Wang, F. Xiong, S. Wang, and Y. Cui, Nano Letters **15**, 1031 (2015), pMID: 25590995, https://doi.org/10.1021/nl503897h.

[74] E. M. Alexeev, D. A. Ruiz-Tijerina, M. Danovich, M. J. Hamer, D. J. Terry, P. K. Nayak, S. Ahn, S. Pak, J. Lee, J. I. Sohn, M. R. Molas, M. Koperski, K. Watanabe, T. Taniguchi, K. S. Novoselov, R. V. Gorbachev, H. S. Shin, V. I. Fal'ko, and A. I. Tartakovskii, Nature **567**, 81 (2019).

[75] E. M. Alexeev, C. M. Purser, C. M. Gilardoni, J. Kerfoot, H. Chen, A. R. Cadore, B. L. Rosa, M. S. G. Feuer, E. Javary, P. Hays, K. Watanabe, T. Taniguchi, S. A. Tongay, D. M. Kara, M. Atatüre, and A. C. Ferrari, Nano Letters **24**, 11232 (2024), pMID: 39213644, https://doi.org/10.1021/acs.nanolett.4c02635.

[76] E. M. Alexeev, A. Catanzaro, O. V. Skrypka, P. K. Nayak, S. Ahn, S. Pak, J. Lee, J. I. Sohn, K. S. Novoselov, H. S. Shin, and A. I. Tartakovskii, Nano Letters **17**, 5342 (2017), pMID: 28753319, https://doi.org/10.1021/acs.nanolett.7b01763.

[77] P. Merkl, F. Mooshammer, P. Steinleitner, A. Girnghuber, K.-Q. Lin, P. Nagler, J. Holler, C. Schüller, J. M. Lupton, T. Korn, S. Ovesen, S. Brem, E. Malic, and R. Huber, Nature Materials **18**, 691 (2019).

[78] T. Deilmann and K. S. Thygesen, Nano Letters **18**, 2984 (2018).

[79] C. Gong, H. Zhang, W. Wang, L. Colombo, R. M. Wallace, and K. Cho, Applied Physics Letters **103**, 053513 (2013).

[80] J. Kang, S. Tongay, J. Zhou, J. Li, and J. Wu, Applied Physics Letters **102**, 012111 (2013).

[81] Y. Wang, Z. Wang, W. Yao, G.-B. Liu, and H. Yu, Phys. Rev. B **95**, 115429 (2017).

[82] C. Zhang, C.-P. Chuu, X. Ren, M.-Y. Li, L.-J. Li, C. Jin, M.-Y. Chou, and C.-K. Shih, Science Advances **3**, e1601459 (2017), https://www.science.org/doi/pdf/10.1126/sciadv.1601459.

[83] D. Kozawa, A. Carvalho, I. Verzhbitskiy, F. Giustiniano, Y. Miyauchi, S. Mouri, A. H. Castro Neto, K. Matsuda, and G. Eda, Nano Letters **16**, 4087 (2016), https://doi.org/10.1021/acs.nanolett.6b00801.

[84] K. L. Seyler, P. Rivera, H. Yu, N. P. Wilson, E. L. Ray, D. G. Mandrus, J. Yan, W. Yao, and X. Xu, Nature **567**, 66 (2019).

[85] K. Tran, G. Moody, F. Wu, X. Lu, J. Choi, K. Kim, A. Rai, D. A. Sanchez, J. Quan, A. Singh, J. Embley, A. Zepeda, M. Campbell, T. Autry, T. Taniguchi, K. Watanabe, N. Lu, S. K. Banerjee, K. L. Silverman, S. Kim, E. Tutuc, L. Yang, A. H. MacDonald, and X. Li, Nature **567**, 71 (2019).

[86] J. Kunstmann, F. Mooshammer, P. Nagler, A. Chaves, F. Stein, N. Paradiso, G. Plechinger, C. Strunk, C. Schüller, G. Seifert, D. R. Reichman, and T. Korn, Nature Physics **14**, 801 (2018).

[87] P. K. Nayak, Y. Horbatenko, S. Ahn, G. Kim, J.-U. Lee, K. Y. Ma, A.-R. Jang, H. Lim, D. Kim, S. Ryu, H. Cheong, N. Park, and H. S. Shin, ACS Nano **11**, 4041 (2017), pMID: 28363013, https://doi.org/10.1021/acsnano.7b00640.

[88] H. Heo, J. H. Sung, S. Cha, B.-G. Jang, J.-Y. Kim, G. Jin, D. Lee, J.-H. Ahn, M.-J. Lee, J. H. Shim, H. Choi, and M.-H. Jo, Nature Communications **6**, 7372 (2015).

[89] F. Wu, T. Lovorn, and A. H. MacDonald, Phys. Rev. Lett. **118**, 147401 (2017).

[90] A. M. van der Zande, J. Kunstmann, A. Chernikov, D. A. Chenet, Y. You, X. Zhang, P. Y. Huang, T. C. Berkelbach, L. Wang, F. Zhang, M. S. Hybertsen, D. A. Muller, D. R. Reichman, T. F. Heinz, and J. C. Hone, Nano Letters **14**, 3869 (2014), pMID: 24933687.

[91] P. Tscheppe, J. Zang, M. Klett, S. Karakuzu, A. Celarier, Z. Cheng, C. A. Marianetti, T. A. Maier, M. Ferrero, A. J. Millis, and T. Schäfer, Proceedings of the National Academy of Sciences **121**, e2311486121 (2024), https://www.pnas.org/doi/pdf/10.1073/pnas.2311486121.

[92] M. Förg, A. S. Baimuratov, S. Y. Kruchinin, I. A. Vovk, J. Scherzer, J. Förste, V. Funk, K. Watanabe, T. Taniguchi, and A. Högele, Nature Communications **12**, 1656 (2021).

[93] V. Crépel and A. Millis, Phys. Rev. Res. **6**, 033127 (2024).

[94] T. Rakib, P. Pochet, E. Ertekin, and H. T. Johnson, Journal of Applied Physics **132**, 120901 (2022).

[95] T. Devakul, V. Crépel, Y. Zhang, and L. Fu, Nature Communications **12**, 6730 (2021).

[96] A. Ramos-Alonso, B. Remez, D. Bennett, R. M. Fernandes, and H. Ochoa, Phys. Rev. Lett. **134**, 026501 (2025).